PROCESSING, MORPHOLOGY, AND MECHANICAL PROPERTIES OF HIGH VOLUME FRACTION ALIGNED CARBON NANOTUBE/AEROSPACE-GRADE EPOXY NANOCOMPOSITES

A. L. Kaiser[1], Luiz H. Acauan[2], I. V. Albelo[3], J. L. Gair Jr.[4], and B. L. Wardle[5]
[1]Department of Materials Science and Engineering, Massachusetts Institute of Technology, Cambridge, MA 02139 U.S.A., Web: mit.edu/~kaisera, alkaiser@alum.mit.edu
[2]Department of Aeronautics and Astronautics, Massachusetts Institute of Technology, Cambridge, MA 02139 U.S.A., Web: aeroastro.mit.edu, lacauan@mit.edu
[3]Department of Aeronautics and Astronautics, Massachusetts Institute of Technology, Cambridge, MA 02139 U.S.A., Department of Materials Science and Engineering, University of California, San Diego, La Jolla, CA 92093 U.S.A., Web: aeroastro.mit.edu, ialbelo@uscd.edu
[4]Department of Aeronautics and Astronautics, Massachusetts Institute of Technology, Cambridge, MA 02139 U.S.A., Institute for Soldier Nanotechnologies, Cambridge, MA 02139 U.S.A.; U.S. Army Research Laboratory, RDRL-VTM, Aberdeen Proving Ground, MD 21005 U.S.A., Currently: Scinetics, Inc., 2915 Islay Court, Abingdon, MD 21009 U.S.A., Web: scineticsinc.com, j.gair.jr@scineticsinc.com
[5]Department of Aeronautics and Astronautics, Massachusetts Institute of Technology, Cambridge, MA 02139 U.S.A., Department of Mechanical Engineering, Massachusetts Institute of Technology, Cambridge, MA 02139 U.S.A., Web: aeroastro.mit.edu, wardle@mit.edu

Keywords: *Carbon nanotubes, Nanocomposites, Nano-engineered, Mechanical properties*

ABSTRACT

Polymer matrix nanocomposites (PNCs) incorporating high volume fractions (V_f in excess of 10 vol%) of aligned carbon nanotubes (A-CNTs) are promising for high-performance structural composite applications leveraging texture for multifunctionality and performance-to-weight ratios. However, to enable the manufacturing of scalable structures using A-CNT PNCs, nanoscale confinement and interfacial effects due to high A-CNT content in aerospace-grade polymer matrices need to be better understood. Here, we report the fabrication of high-V_f CNT PNCs to develop process-structure-property relationships, notably to fabricate microvoid-free and fully infused CYCOM 977-3 epoxy PNCs with high packing densities of biaxially mechanically densified millimeter-tall A-CNT array reinforcement (1-30 vol% corresponding to average inter-CNT spacings of ~70 to 6 nm) via capillary- and vacuum-assisted resin infusion. Microvoid-free PNCs are confirmed via X-ray microcomputed tomography and scanning electron microscopy, where a diluted resin with ~10× lower viscosity than a neat resin is required to obtain complete infusion into high- V_f A-CNT arrays (10-30 vol%). Raman spectroscopy indicates that atomic-scale defect density decreases at higher CNT packing fractions and upshifts in the Raman D- and G-bands are observed at increasing V_f. The CNTs contribute more to the Raman spectra compared to the amorphous polymer matrices at high CNT V_f due to their higher concentration in the matrix. Finally, a ~2× increase in the axial indentation modulus for 30 vol% A-CNT PNCs compared to that of the neat resin is measured, and no significant change in the transverse A-CNT modulus is shown experimentally and via modeling, indicating that reinforcement with A-CNTs at higher V_f values leads to enhanced anisotropic mechanical properties. Through the process-structure-property scaling relationships established here, this work supports the development of next-generation structures comprised of nanomaterials with enhanced performance and manufacturability.

1 INTRODUCTION

The advantaged intrinsic and mass-specific properties of aligned carbon nanotubes (A-CNTs) and their facile densification into uniformly high-volume fraction (V_f) arrays motivates their use as dense aerospace composite reinforcement [1-5]. Since tuning A-CNT array packing density is essential for improving properties such as strength, toughness, and conductivity for both polymer nanocomposites

(PNCs) [1-4] and advanced composite laminates [5], it is necessary to understand how the processing and multi-scale structure of aerospace-grade polymer matrices are affected by A-CNT confinement (*i.e.* high CNT V_f with inter-CNT spacings on the order of nanometers [2,6]). To provide deeper insight into these phenomena, this study presents experimental process-structure-property relations to detail how CNT V_f up to 30 vol% in mesoscale aligned CNT arrays influences processing, morphology, and mechanical behavior of PNCs, supporting the design and fabrication of next-generation composites.

In this work, multiwalled aligned CNT-epoxy PNCs are created by infusing aerospace-grade 977-3 epoxy resin [6-8] into mm-tall A-CNT arrays ranging from 1-30 vol%. The A-CNT arrays are synthesized *via* chemical vapor deposition on Si wafers, then are delaminated from their substrate with a razor blade, mechanically densified from 1 to 30 vol% V_f (yielding inter-CNT spacings of ~70 to 5 nm [2,6]), infused with neat epoxy resin *via* vacuum-assisted capillary-driven wetting (where a diluted 65 wt% resin/acetone solution is used for 10-30 vol% arrays), and cured. The PNCs are characterized as a function of CNT V_f *via* X-ray micro-computed tomography (μCT) and scanning electron microscopy (SEM), Raman spectroscopy, and nanoindentation testing in both axial and transverse CNT orientations for microtomed PNCs. These analyses provide multi-scale information regarding epoxy infiltration and morphology, polymer and CNT structure, and mechanical properties, respectively.

2 METHODS

2.1 CNT Growth and Densification to High V_f Values (1–30 Vol%)

Vertically aligned CNT arrays with heights of 2 mm (for 1-20 vol% A-CNT PNCs) and 1 mm (for 30 vol% A-CNT PNCs) were synthesized in a 22 mm internal size quartz tube furnace via a previously described thermal catalytic CVD process, which uses ethylene as the carbon source and water vapor added to inert helium gas [4,7]. The CNTs were grown on 1 cm × 1 cm Si wafer substrates via a base-growth mechanism on a catalyst layer, which is composed of 1 nm Fe on 10 nm Al_2O_3 deposited via electron-beam physical vapor deposition. During growth, the CNTs self-assemble into vertically aligned arrays composed of multiwalled CNTs with an average outer diameter of ~9 nm (3-7 walls with ~5 nm inner diameter and an intrinsic CNT density of ≈1.6 g/cm^3), Γ values of ~60-80 nm, and CNT V_f of ~1 vol% CNTs [2,4,7]. A postgrowth 4 min H_2 thermal treatment [8] was used to weaken the CNT-catalyst attachment, which allows for easy delamination of the CNT array from the silicon substrate using a razor blade, thereby enabling A-CNT array processing in a free-standing state. A-CNT array samples were then densified via a biaxial mechanical densification process (see Figure 1). A free-standing as-grown A-CNT array was placed in a device made of Teflon and using steel compression rods that permits biaxial compression (densification) in two orthogonal directions, with the final CNT V_f calculated as the ratio of the initial CNT array area to the densified CNT array area. The CNT V_f will range from 1 to 5, 10, 20, and 30 vol% with Γ values of ~70 to 6 nm, corresponding to square array dimensions of ~1.0 cm^2 and 1.82 mm^2, respectively [7].

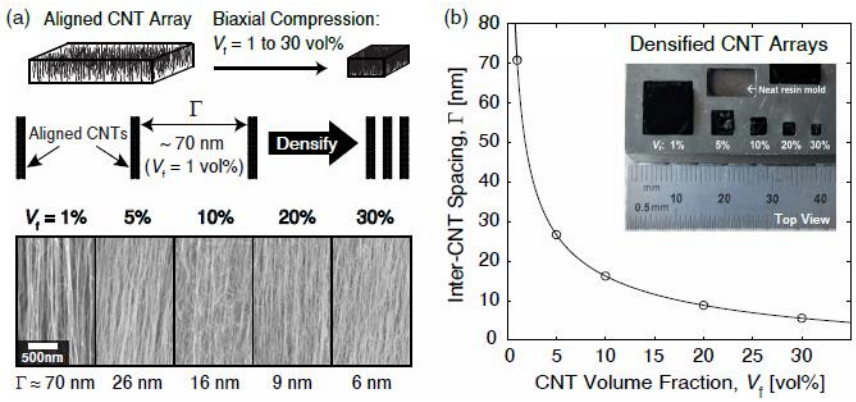

Figure 1: Overview of the densification of vertically aligned CNT arrays from 1 to 30 vol% for use as densified composite reinforcement: (a) Aligned CNT biaxial mechanical compression increases the

CNT volume fraction (V_f) from 1 vol% (as-grown arrays) to 30 vol%, which decreases the inter-CNT spacing (Γ) from ~70 to 6 nm while maintaining vertical CNT alignment as shown by exemplary SEM images of densified A-CNT arrays at each CNT V_f, adapted from Kaiser et al. [6] (b) Scaling of the inter-CNT spacing with CNT V_f assuming square packing, as adapted from Wardle et al., [2] and top-down view optical micrograph of the densified CNT arrays in a steel mold.

2.2 Fabrication of Aligned CNT PNCs via Capillary-Driven Infusion and Curing of Epoxy Resin

To fabricate A-CNT PNCs from aerospace-grade resin (CYCOM 977-3 epoxy resin from Solvay), a free-standing CNT array with 1-30 vol% CNT V_f was first placed in a steel mold matching its dimensions so that the longitudinal axis of the CNTs was orthogonal to the plane of the mold (see Figure 2) [6-8]. Before CNTs were added, the mold was first coated in mold release (Loctite Frekote 700-NC). Then, uncured liquid prepolymer (the unmodified epoxy resin) was heated to 100°C in glass beakers for 5 h degassing in a vacuum oven. The neat resin was then heated to 120°C for infusion, and then poured into the 1 and 5 vol% molds to create low CNT V_f PNCs, where resin infusion into the A-CNTs occurred for 2 h at 120°C under vacuum. For high-V_f CNT PNCs, 65 wt% resin solutions were made by sonicating the uncured resin in acetone at room temperature for 30 min, and then this solution was poured into the 10–30 vol% molds for up to 3 h of capillary-assisted infusion at room temperature. After infusion, the PNCs were dried to remove acetone at 80°C for 2 h under vacuum [7,8]. To obtain the final cured PNC samples for each CNT V_f, the infused A-CNT arrays were cured following the manufacturer's cure cycle (177°C for 6 h) [7,8].

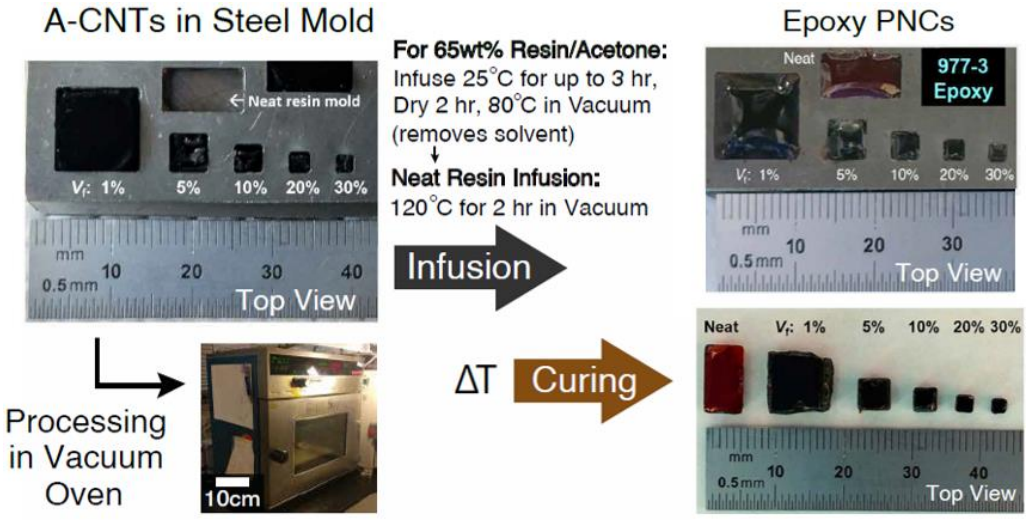

Figure 2: Fabrication overview of the fabrication of aligned CNT-polymer matrix nanocomposites (PNCs), where 1-30 vol% A-CNT arrays are infused with an aerospace-grade 977-3 epoxy resin matrix: (a) Side-view schematics of neat uncured resin infusion and curing in a steel mold. (b) Top-down view optical micrographs of A-CNT arrays before and after resin infiltration and curing in a vacuum oven following the manufacturer's recommended cure cycle, where the resin is infused via the vacuum-assisted capillary-driven wetting of A-CNT arrays. (c) Top-down view optical micrographs of the final cured A-CNT epoxy PNCs at each CNT V_f, including a cured neat resin baseline.

2.3 Morphological Characterization: SEM and X-ray µCT Imaging

High resolution SEM was used to characterize the morphology and fracture surfaces of the PNCs, which were mechanically hand-fractured at room temperature along the primary CNT axis using a razor blade. SEM was performed using a Zeiss Merlin scanning electron microscope with a 5 mm working distance and 5 kV accelerating voltage. In addition, X-ray µCT is a useful non-destructive imaging technique that is employed here to provide 2D cross-section slices and 3D bulk volume rendering of the

PNC interior, which allows for visualization of the polymer infiltration extent at the micro-scale. X-ray μCT scans were conducted on the cured PNC samples and cured neat resin using a Zeiss Xradia 520 Versa X-ray microscope with a source voltage of 60 kV. A total of 1601 radiograph projections were acquired at a 2 μm isotropic voxel size (~4-5 μm resolution) with a 3 s exposure time with each sample centered in the field of view (4 mm × 4 mm × 4 mm). Analysis of the 3D volumes was performed using the Zeiss Reconstructor Scout-and-Scan Software and Dragonfly 4.1 program [7,8]. Figures 3-4 show SEM images of the PNC fracture surfaces, and Figure 3 shows the 3D and 2D X-ray μCT images as a function of CNT V_f. In addition, each material constituent (30 vol% A-CNT array, 30 vol% A-CNT/epoxy PNC, and cured neat resin) were scanned together following the same parameters as described above, and these results are shown in Figure 3.

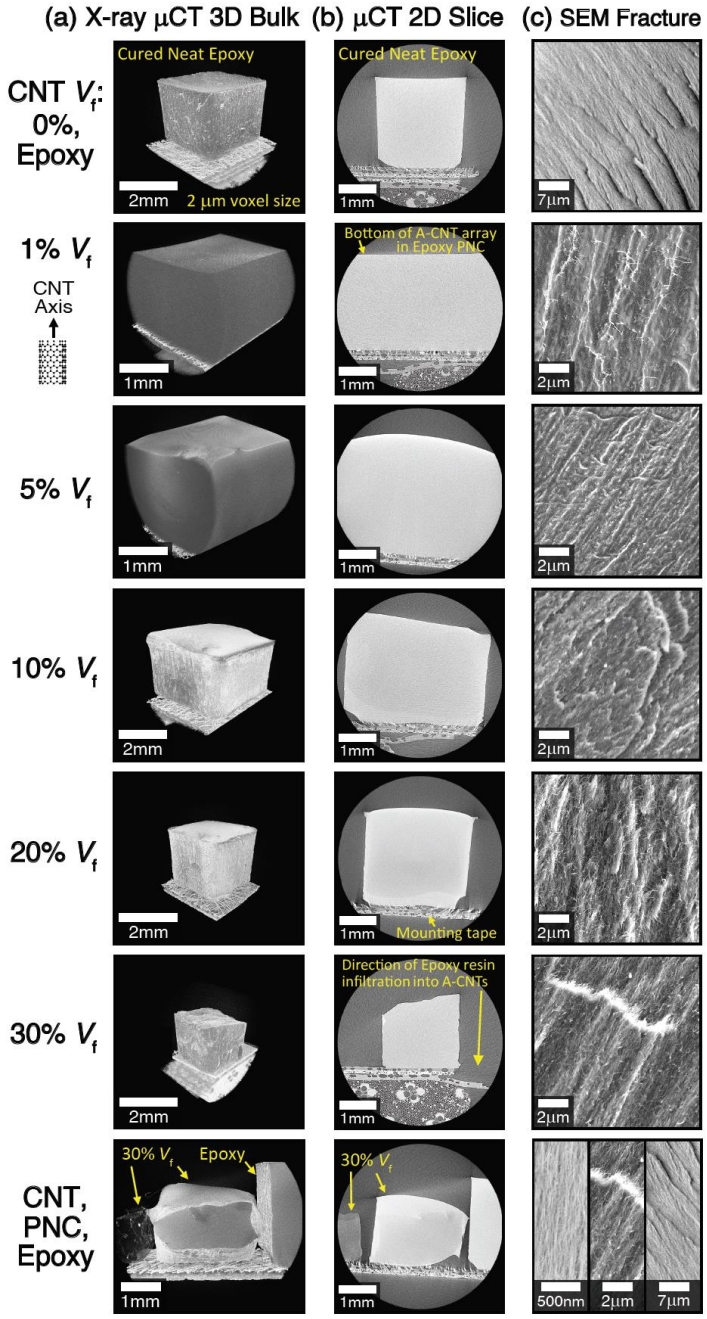

Figure 3: Visualization of fully infiltrated and cured CNT-epoxy PNCs via (a) 3D bulk X-ray μCT images, (b) 2D X-ray μCT slices of the cross section (2 μm voxel size), and (c) SEM images of the room temperature hand-fracture surfaces as a function of CNT V_f. This imaging analysis shows no

microvoids, a uniform density, maintained CNT alignment and dispersion, thorough CNT-epoxy wetting, and CNT pullout from the matrix as a result of fracture for each CNT V_f. At the bottom, a compilation of X-ray μCT images compares the constituents in epoxy PNCs, showing (from left to right in each image) a 30 vol% aligned CNT array, 30 vol% CNT-epoxy PNC, and cured neat epoxy baseline scanned within the same field of view (2 μm voxel size).

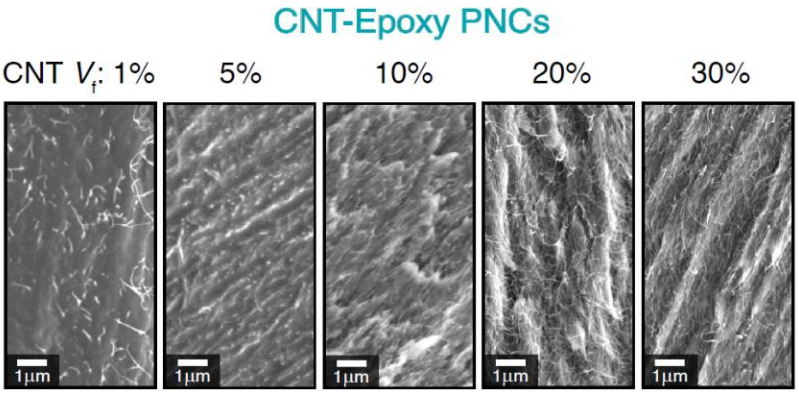

Figure 4: SEM images of the fracture surfaces of fully infused and cured 1-30 vol% CNT V_f CNT-epoxy PNCs resulting from room temperature mechanical hand-fracture, showing thorough CNT-polymer wetting, maintained alignment, CNT bridging, and pull-out from the matrix at each CNT V_f. Note that the CNT orientation in the SEM images of fracture is now known given sample preparation.

2.3 Structural Characterization: Raman Spectroscopy

Raman spectroscopy is used to quantify the atomic-scale structural changes and bonding character evolution in the cured CNT-epoxy PNCs, cured neat resin, and as-grown A-CNTs as a function of CNT V_f, as this technique is broadly used to analyze defect densities and disorder in carbon-based materials. Raman spectra were collected using a LabRam HR800 Raman microscope (Horiba Jobin Yvon) with 633 nm (1.96 eV) laser excitation through a 50x objective and LabSpec6 software. At least 3 spots on each sample (for at least 2 samples of each type) were studied to ensure that representative data could be used to analyze the Raman D- 2D-, and G-bands characteristic of carbon materials. In addition, the 633 nm laser allows the G+ and G- modes of the G-band to be visualized in CNTs (here consistent across all CNT V_f), which arise due to the longitudinal and transverse optical phonons in the Raman scattering of CNTs [9,10].

To quantify the change in Raman shift for each band as a function of CNT V_f, the bands were fit with mixed Gaussian/Lorentzian peaks using the Levenberg-Marquardt algorithm, and the G+ and G- components of the G-band for CNT-based samples had their position correlated by a fixed 34.5 cm^{-1} shift between these components, in accordance with prior work and experimentally measured spectra [11]. The average Raman shift location (in cm^{-1}) of the two G-bands was then calculated to compare the overall G-band Raman shift evolution (*i.e.* change in the location of the band) with increasing CNT V_f. The evolution of the D-band and 2D-band Raman shifts with CNT V_f were also determined by the Raman shift where the maximum intensity of the fitted D- or 2D-band was located for each CNT V_f, and each of the metrics described here were not affected by CNT direction. Representative Raman spectra and fits for the as-grown A-CNT arrays, cured neat epoxy samples, and CNT-epoxy PNCs as a function of CNT V_f are presented in Figure 5.

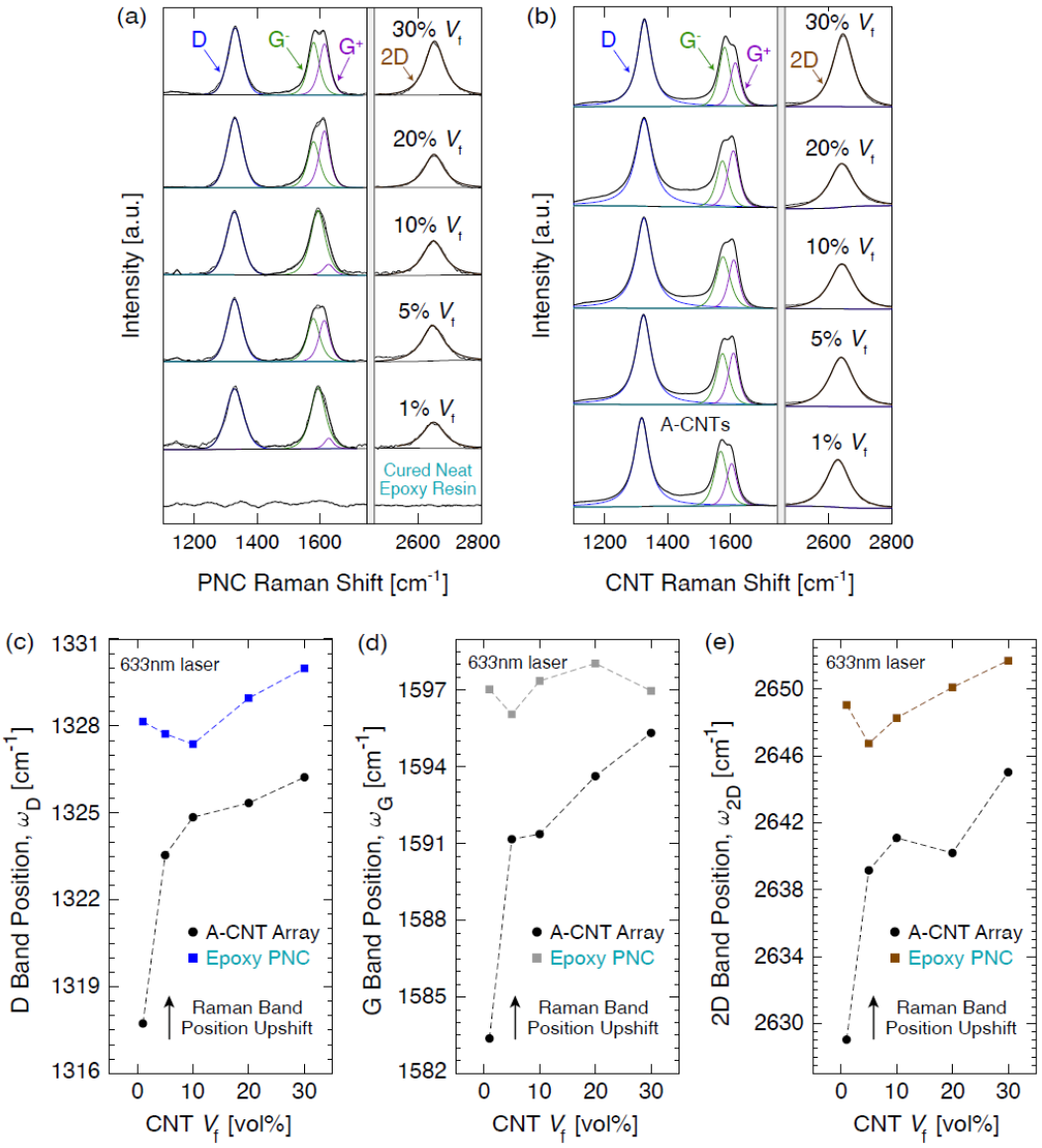

Figure 5: Representative Raman spectra for: (a) neat resin and CNT-epoxy PNCs and (b) as-grown aligned CNT arrays showing the evolution of the characteristic carbon D-, G-, and 2D-bands as a function of CNT V_f (633 nm laser). Significant Raman upshifts (≳10 cm^{-1}) in the (c) D-band, (d) G-band, and (e) 2D-band positions are observed with CNT densification prior to incorporation into the PNCs, and shifts are also noted after infusion and curing, indicating that the wavy as-grown CNTs can straighten and exhibit a ≳2× decrease in waviness ratio at increasing CNT V_f up to 30 vol%.

2.5 Mechanical Property Characterization: Nanoindentation Testing

To understand how increased A-CNT reinforcement in epoxy matrices affects the mechanical properties of these nanocomposites, and the local quasi-static mechanical properties and the anisotropy ratio between axial and transverse CNT orientations, microstructural mechanical characterization was performed using nanoindentation. To prepare the cured neat resin and PNCs for nanoindentation testing, room temperature ultramicrotoming of the samples was performed using a Leica Ultramicrotome to yield smooth surfaces in the axial and transverse CNT directions of the PNCs with sample thicknesses of >500 μm, as shown in Figure 6 [7,8]. Then, nanoindentation testing was performed with a Hysitron TI 950 TriboIndenter by indenting a 7 × 7 grid on two samples of each type using a diamond Berkovich tip with a radius of curvature of 150 nm. Testing was performed on cured neat epoxy and epoxy PNC

samples in the axial and transverse CNT directions [7,8]. Force control (up to 10 mN) was applied via a trapezoidal load function, yielding an indentation depth of ~1 μm. This loading function resulted in quasi-static loading, allowed stabilization of the specimen during the hold period, unloaded quasi-statically, and gave a maximum area of indentation of ≳20 μm^2 and an indentation depth of ~1 μm to minimize noise in measurements. Therefore, this nanoindentation testing engages ≳5000 CNTs in the indentation of 1 vol% PNCs, and ≳700000 CNTs in the indentation of 30 vol% PNCs to capture CNT reinforcement effects on the PNC's indentation modulus [8]. The scaling of the axial and transverse indentation modulus and anisotropy ratio with CNT V_f are shown in Figure 7 and Table 1, including an anelastic correction that accounts for non-negligible viscous deformation during unloading, as discussed as part of the nanoindentation analysis in Section 3.3.

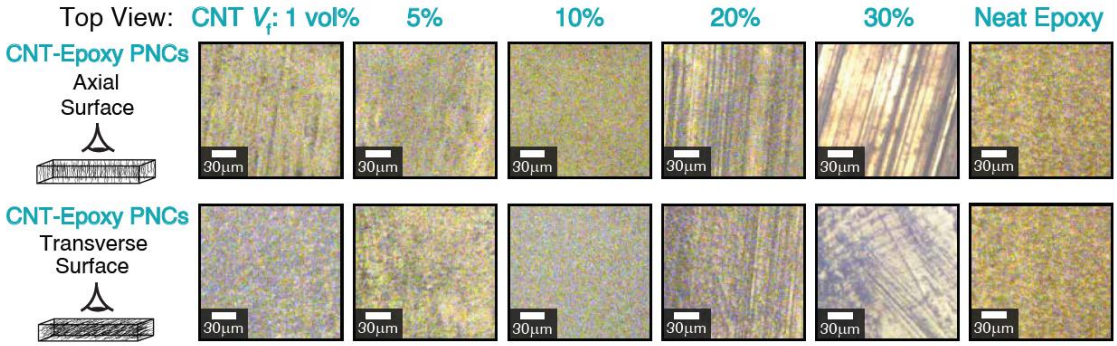

Figure 6: Top-down view optical micrographs and schematics of the ultramicrotomed surfaces for cured neat resin and CNT-epoxy PNCs, in both the axial and transverse CNT orientations. Microtoming the samples either perpendicular to or along the direction of the primary CNT axis results in ultra-smooth surfaces for nanoindentation testing in the axial and transverse CNT orientations, respectively.

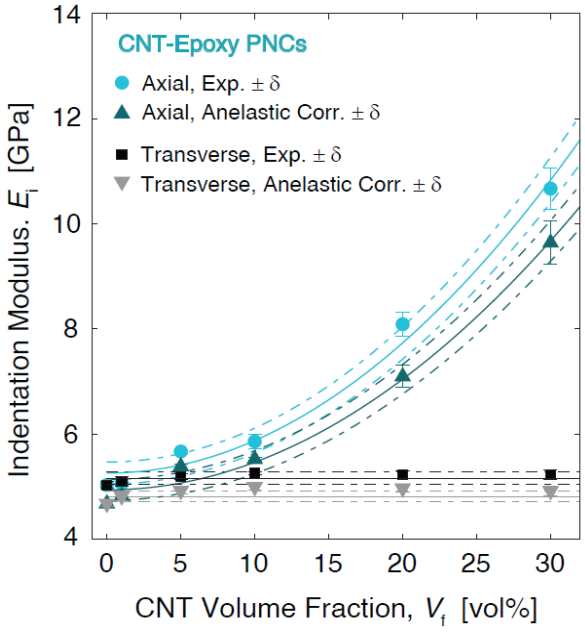

Figure 7: Scaling of the axial and transverse indentation modulus with CNT V_f for CNT-epoxy PNCs, incorporating the anelastic correction that accounts for viscoelastic effects during unloading. This effect reduces the indentation moduli by ~7% for both the axial and transverse CNT orientations in the PNCs as well as the neat resin, while preserving the power-law scaling of axial indentation modulus with CNT V_f.

Table 1: Experimentally determined indentation modulus with standard error for the axial ($E_{i,A}$) and transverse ($E_{i,T}$) CNT orientations in aligned CNT-epoxy nanocomposites and the anisotropy ratio ($E_{i,A}/E_{i,T}$) as a function of CNT volume fraction (CNT V_f), as measured via nanoindentation testing, as well as the indentation moduli and anisotropy ratio with the anelastic corrections ($E_{i,A,corr}$, $E_{i,T,corr}$, and $E_{i,A,corr}/E_{i,T,corr}$).

V_f [vol%]	0 (Epoxy)	1	5	10	20	30
$E_{i,A}$ [GPa]	5.030 ± 0.06	5.063 ± 0.03	5.669 ± 0.03	5.887 ± 0.14	8.041 ± 0.22	10.67 ± 0.40
$E_{i,T}$ [GPa]	5.030 ± 0.06	5.097 ± 0.10	5.187 ± 0.06	5.253 ± 0.03	5.224 ± 0.07	5.232 ± 0.09
$E_{i,A}/E_{i,T}$	~1	~0.993	~1.09	~1.12	~1.54	~2.04
$E_{i,A,corr}$ [GPa]	4.678 ± 0.06	4.819 ± 0.04	5.384 ± 0.04	5.521 ± 0.04	7.095 ± 0.21	9.639 ± 0.41
$E_{i,T,corr}$ [GPa]	4.678 ± 0.06	4.818 ± 0.09	4.924 ± 0.06	4.997 ± 0.06	4.970 ± 0.08	4.919 ± 0.09
$E_{i,A,corr}/E_{i,T,corr}$	~1	~1	~1.09	~1.11	~1.43	~1.96

3 RESULTS AND DISCUSSION

3.1 SEM and X-ray μCT Analysis

The SEM micrographs of the PNCs in Figures 3-4 can be analyzed to investigate how CNT confinement influences polymer infusion, wetting, CNT dispersion, and the overall CNT-matrix morphology, especially the CNT alignment in the matrix and the PNC microstructure after curing. SEM also details the cross-sectional fracture surfaces that show the fracture behavior for each polymer, such as CNT bridging and pull-out from the matrix, indicating qualitatively the relative strength of CNT-matrix interactions based on CNT V_f. The SEM micrographs of these PNC fracture surfaces show that the polymer matrices fill the spaces between the A-CNTs for each CNT V_f up to 30 vol%, and wetting is achieved even for 30 vol%, which is the smallest inter- CNT spacing tested. The A-CNTs also maintain their alignment and dispersion in the matrix upon resin infusion and curing. Further, the SEM images show that PNC fracture behavior is dominated by CNT bridging and pull-out/debonding from the matrix The CNTs exhibit pull-out here due to interfacial debonding from the polymer matrix as the CNTs and polymer resist the applied load, and therefore failure is governed by the relative adhesion of the polymer to the A-CNTs in the composite. This analysis gives a qualitative indication of the relative strength of CNT-matrix interactions and pull-out behavior based on CNT V_f. The X-ray μCT images in Figure 3 confirm full resin infiltration into the 1-30 vol% CNT V_f A-CNT arrays at the micron scale for the epoxy resin, which is evidenced by the consistent gray color across each PNC denoting uniform density and no microvoids within the PNC slices, consistent with the X-ray μCT images of the cured neat resin.

3.2 Raman Spectroscopy Analysis

The dominant spectral features in the A-CNT and PNC Raman spectra shown in Figure 5 include the Raman D-band, which is found at a Raman shift of ~1315–1340 cm^{-1} and represents carbon defects and structural disorder in the (002) plane and breathing modes of sp^2 atoms in rings, the Raman G-band, which is found at ~1580–1600 cm^{-1} and signifies in-plane sp^2 bond stretching in rings and chains, and the Raman 2D-band, which is a signature of graphitic sp^2 materials and represents the second order of the D-band [12]. Polymer Raman bands were evaluated at ~1190 cm^{-1}, ~1450 cm^{-1}, and ~1614 cm^{-1}, corresponding to C-C stretching and C=C aromatic chain vibrations in the cured polymer [13-15]. The intensity ratios of the carbon D-, 2D-, and G-bands (I_D/I_G) and (I_{2D}/I_G) and the band locations (*i.e.* Raman shifts) in the CNTs and PNCs were compared here to determine the relative defect density, structural order, and strain to study PNC structural evolution as a function of epoxy infusion into high CNT V_f A-CNT arrays. Figure 5 shows that significant Raman upshifts ($\gtrsim$10 cm^{-1}) in the D-band, G-band, and 2D-band positions are observed with CNT densification prior to incorporation into the PNCs, and shifts are also seen after polymer infusion [4,16], indicating that the wavy as-grown CNTs can straighten and exhibit a $\gtrsim$2× decrease in waviness ratio at increasing CNT V_f up to 30 vol% [17]. Raman spectra in

Figure 5 show that the crystalline CNT structure is maintained upon polymer infusion and curing, as expected. Here, the D-, 2D-, and G-bands of the high crystallinity CNTs are well defined, and as CNT V_f increases, these bands dominate the spectra compared to the polymer bands. The Raman spectra are interpreted as being a superposition of the CNT and epoxy bands, as no new bands appear when CNT V_f increases through 30 vol%, and the polymer bands are only slightly visible in the 1 vol% CNT V_f spectra. Significant CNT intensity contributes at CNT $V_f \gtrsim$1-5 vol% consistent with prior work on similar material systems [13-15].

In addition, I_D/I_G remains approximately constant with CNT V_f in the epoxy PNCs, signifying that CNT-polymer confinement effects at small inter-CNT spacings are not present in the PNCs. The I_{2D}/I_G ratio increases steadily with CNT V_f for the epoxy PNCs, which is expected to result from the higher crystallinity CNTs contributing more to the Raman spectra than the amorphous polymer matrices at higher CNT packing fractions. While the intensity ratios of the bands quantify the relative defect density in the samples, the Raman band locations (*i.e.* Raman shift, or wavenumber) can qualitatively and quantitatively indicate potential strain on the CNTs within the PNCs as a result of the composite fabrication process. A ~10 cm^{-1} upshift in the D- and G-bands is observed for a 1 vol% PNC compared to a 1 vol% A-CNT array with no polymer. This indicates that the A-CNTs may straighten during the biaxial mechanical densification to exhibit a lower waviness ratio than for their as-grown case [17], shifting the Raman band location, and that polymer infusion into A-CNTs can also lead to waviness decreases in addition to confinement effects due to densification. During PNC fabrication (*i.e.* curing at elevated temperature and then cooling to room temperature), internal residual compressive stresses can be generated due to cure shrinkage of the polymer and mismatch between the coefficients of thermal expansion for the polymer and CNTs, which can produce a local compressive strain on the CNT walls within the composite to yield the observed upshift in the Raman band location, as noted in previous studies [18-19]. This phenomenon is consistent with the thorough wetting and polymer infusion seen via SEM, prior work that showed a 3 cm^{-1} Raman G-band upshift for ~5 wt% CNT-epoxy PNCs compared to pure CNTs [19], Raman G- and 2D-band upshifts for compressive strain applied to graphene [20], and a past study reporting a downshift in the Raman G-band when a tensile axial strain was applied to suspended CNTs [18].

3.3 Nanoindentation Analysis

For both the epoxy PNCs tested via nanoindentation, the transverse force-displacement curves exhibit a similar mechanical response at all CNT V_f (due to being polymer matrix-dominated) [4,16], while the axial curves show a significantly enhanced mechanical response as CNT V_f increases from 0 to 30 vol% (*i.e.* a smaller maximum indentation depth with a larger slope at the point of unloading). This results in a ~2× increase in the axial indentation modulus and axial/transverse anisotropy ratio for 30 vol% CNTs compared to the cured neat resin: ~5.0 to 10.67 GPa in epoxy PNCs, as shown in Figure 7 and Table 1. The mechanism responsible for this behavior is attributed to the columnar compression of the A-CNTs along their longitudinal axis to capture their enhanced stiffness in this orientation, and this is consistent with how the CNTs contribute more to the overall PNC mechanical response at higher CNT V_f and when they are oriented axially as compared to transversely during indentation testing. The axial indentation moduli for 30 vol% PNCs are still less than rule of mixtures estimates (>100 GPa for 1 TPa stiffness CNT walls) [16] due to the known CNT waviness effects governing mechanical behavior that can reduce the effective elastic axial modulus of A-CNT arrays by several orders of magnitude [4,16-17,22-23]. In addition, the axial indentation modulus exhibits highly non-linear, power-law scaling with CNT V_f in the PNCs (quadratic scaling fit for epoxy PNCs as shown in Eq. 1, where R^2 = 0.99). This is similar to the power-law scaling of the axial indentation modulus with CNT V_f that was observed for neat A-CNT arrays [8,17] and highly non-linear scaling for A-CNT/epoxy PNCs previously measured up to 20 vol% [22-23]. These results are attributed to the reductions in CNT waviness at high CNT V_f by up to a factor of 2 [4,16-27], commensurate with a higher contribution of CNT reinforcement to the overall PNC mechanical response with higher CNT V_f.

$$E_{i,A,Epoxy} = 6.191 \times 10^{-3}(V_f)^2 + 5.258 \quad (1)$$

Furthermore, since the calculation of indentation modulus uses the Oliver-Pharr method that assumes purely elastic behavior during unloading [24], which may not be fully accurate if the samples undergo non-negligible viscous deformation [24-25]. An anelastic correction was applied following prior work [25] to account for these effects and correct for their potential reductions to the indentation modulus (see additional details and Python scripts by Gair) [25]. To do so, the rate of change in displacement just prior to the end of the hold segment, and the rate of change in load at the beginning of unloading is calculated and used to find the anelastic corrected reduced stiffness based on prior work on similar polymers, including epoxy [25]. This correction yields a slightly lower indentation modulus, because materials with larger creep lead to a higher rate of change of displacement during indentation testing. Anelastic corrected indentation moduli scaling with CNT V_f for the epoxy PNCs are presented in Figure 7, along with the original indentation moduli. This correction leads to a relatively small (~7%) decrease in the indentation modulus in the axial and transverse CNT orientations for each CNT V_f. Similar power-law scaling of the corrected axial indentation modulus is also observed as a function of V_f, which is shown in Eq. 2 ($R^2 = 0.99$).

$$E_{i,A,corr,Epoxy} = 5.264 \times 10^{-3}(V_f)^2 + 4.938 \quad (2)$$

As shown here, the incorporation of A-CNTs up to 30 vol% in an epoxy matrix can yield up to a ~2× increase in the axial indentation modulus and axial/transverse anisotropy ratio compared to the neat resin, demonstrating the reinforcement potential of A-CNTs in aerospace-grade polymer composites.

4 CONCLUSIONS

In summary, multiwalled A-CNT/aerospace-grade epoxy matrix PNCs with mm-tall densified A-CNT reinforcement were fabricated, and their process-structure-property relationships are analyzed as a function of CNT V_f via SEM, X-ray μCT, Raman spectroscopy, and nanoindentation testing. These analyses provide multi-scale information to show how CNT confinement in dense arrays from 1-30 vol% influences polymer infiltration, wetting, structural evolution, and CNT-matrix morphology, including PNC fracture surfaces. SEM results show that CNT alignment in the matrix is maintained throughout all processing steps, where fractography also reveals evidence of CNT pull-out. The confirmation of complete resin infusion and microvoid-free PNCs is evidenced by SEM and X-ray μCT imaging of the composite interior. Raman spectroscopy indicates that atomic-scale defect density appears to decrease at higher CNT packing fractions, and upshifts in the Raman D- and G-bands are observed at increasing V_f. The CNTs contribute more to the Raman spectra compared to the amorphous polymer matrices at high CNT V_f due to their higher concentration in the matrix. Finally, a ~2× increase in the axial indentation modulus for 30 vol% A-CNT PNCs compared to that of the neat resin is measured, with additional incorporation of anelastic effects during indentation. No significant change in the transverse A-CNT modulus is shown experimentally and via modeling, indicating that reinforcement with A-CNTs at higher V_f values leads to enhanced anisotropic mechanical properties. Through the process-structure-property scaling relationships established here, this work supports the development of next-generation structures comprised of nanomaterials with enhanced performance and manufacturability.

With the capability of fabricating fully infused high-density CNT composites beyond 20 vol%, multifunctional property testing could also now be explored, such as electrical conductivity, thermal conductivity, sensing capabilities toward structural health monitoring applications, and CNT architectures for interlaminar reinforcement in aerospace laminates and other polymer systems such as thermoplastics, where the formation of a polymer interphase may be more likely to occur to study nanoscale confinement and scale the composite performance. In these highly loaded composites that can now be made toward larger scales into bulk nanocomposite laminates [7], tensile and compression mechanical tests, including failure, Fourier transform infrared spectroscopy, and TGA in air can be explored to understand laminate-scale mechanical reinforcement and oxidation resistance for high-performance structural composite applications. Future work should explore these topics and processing methods, especially to determine which yields composites with the ideal combination of physical

properties. The knowledge gained will continue to support the integration of densely packed CNTs for a wide range of applications, such as aerospace polymer composite laminates and nanoengineered hybrid materials with multifunctional properties.

ACKNOWLEDGEMENTS

This work was partially supported by Airbus, ANSYS, Boeing, Embraer, Lockheed Martin, Saab AB, and Teijin Carbon America through MIT's Nano-Engineered Composite aerospace STructures (NECST) Consortium, the National Aeronautics and Space Administration (NASA) Space Technology Research Institute (STRI) for Ultra-Strong Composites by Computational Design (US-COMP), Grant No. NNX17AJ32G, and the U.S. Army Research Laboratory and the U.S. Army Research Office through the Institute for Soldier Nanotechnologies (ISN) under Contract No. W911NF-13-D-0001. A.L.K. was supported by the Department of Defense (DoD) through the National Defense Science and Engineering Graduate Fellowship (NDSEG) Program. μCT instrumentation support by the Office of Naval Research (ONR) under Grant ONR.N000141712068 through the Defense University Research Instrumentation Program (DURIP) and the material donation of epoxy resin to US-COMP by Solvay that supported this work are gratefully acknowledged. This work made use of the MIT MRSEC Shared Experimental Facilities supported by the National Science Foundation under Award No. DMR-0819762, was supported in part by the U.S. Army Research Office through the Institute for Soldier Nanotechnologies at MIT, under Cooperative Agreement No. W911NF-18-2-0048, and was carried out in part through the use of MIT's Microsystems Technology Laboratories. The authors gratefully acknowledge Prof. G. Odegard (MTU), Prof. C. Thompson (MIT), Prof. L. Gibson (MIT), and the members of necstlab for technical support and helpful discussions.

REFERENCES

[1] J. N. Coleman, U. Khan, W. J. Blau, and Y. K. Gun'ko. "Small but strong: A review of the mechanical properties of carbon nanotube–polymer composites". *Carbon*, Vol. 44, pp 1624-1652, 2006. (doi: 10.1016/j.carbon.2006.02.038).

[2] B. L. Wardle, D. S. Saito, E. J. Garcia, A. J. Hart, R. G. de Villoria, and E. A. Verploegen. "Fabrication and characterization of ultralight-volume-fraction aligned carbon nanotube-polymer composites". *Advamced Materials*, Vol. 20, pp 2707, 2008. (doi: 10.1002/adma.200800295).

[3] A. Mikhalchan, T. Gspann, and A. Windle. "Aligned carbon nanotube–epoxy composites: the effect of nanotube organization on strength, stiffness, and toughness". *Journal of Materials Science*, Vol. 51, pp 10005-10025, 2016. (doi: 10.1007/s10853-016-0228-6).

[4] B. Natarajan, I. Y. Stein, N. Lachman, N. Yamamoto, D. S. Jacobs, R. Sharma, J. A. Liddle, and B. L. Wardle. "Aligned carbon nanotube morphogenesis predicts physical properties of their polymer nanocomposites". *Nanoscale*, Vol. 11, pp 16327, 2019. (doi: 10.1039/C9NR03317C).

[5] X. Ni, L H. Acauan, and B. L. Wardle. "Coherent nanofiber array buckling-enabled synthesis of hierarchical layered composites with enhanced strength". *Extreme Mechanics Letters*, Vol. 39, pp 100773-100781, 2020. (doi: 10.1016/j.eml.2020.100773).

[6] A. L. Kaiser, I. V. Albelo, and B. L. Wardle. "Fabrication of aerospace-grade epoxy and bismaleimide matrix nanocomposites with high density aligned carbon nanotube reinforcement". *2020 AIAA SciTech Forum*, Vol. 1, 2256, pp 1-12, 2020. (doi: 10.2514/6.2020-2256).

[7] A. L. Kaiser, C. A. C. Chazot, L. H. Acauan, I. V. Albelo, J. Lee, J. L. Gair Jr., A. J. Hart, I. Y. Stein, and B. L. Wardle. "High-volume-fraction textured carbon nanotube-bis(maleimide) and -epoxy matrix polymer nanocomposites: Implications for high-performance structural composites". *ACS Applied Nano Materials*, Vol. 5, pp 9008, 2022. (doi: 10.1021/acsanm.2c01212).

[8] A. L. Kaiser. "Interfacial and physical confinement effects on the structure and properties of aligned carbon nanotube architectures". Ph.D. Thesis, Massachusetts Institute of Technology, Cambridge, MA, 2021. (https://dspace.mit.edu/handle/1721.1/138960).

[9] H. Telg, M. Fouquet, J. Maultzsch, Y. Wu, B. Chandra, J. Hone, T. F. Heinz, and C. Thomsen. "G- and G+ in the Raman spectrum of isolated nanotube: a study on resonance conditions and lineshape". *Phys. Status Solidi B*, Vol. 245, pp 2189, 2008. (doi: 10.1002/pssb.200879658).

[10] M. Mucha, A. Krzyzak, E. Kosicka, E. Coy, M. Koscinski, T. Sterzynski, and M. Salacinski. "Effect of MWCNTs on wear behavior of epoxy resin for aircraft applications". *Materials*, Vol. 13, pp 2696, 2020. (doi: 10.3390/ma13122696).

[11] R. J. Young, L. Deng, T. Z. Wafy, and I. A. Kinloch. "Interfacial and internal stress transfer in carbon nanotube based nanocomposites". *Journal of Materials Science* Vol 51, pp 344-352, 2016. (doi: 10.1007/s10853-015-9347-8).

[12] P. Mallet-Ladeira, P. Puech, C. Toulouse, M. Cazayous, N. Ratel-Ramond, P. Weisbecker, G. L. Vignoles, and M. Monthioux. "A Raman study to obtain crystallite size of carbon materials: A better alternative to the Tuinstra-Koenig Law". *Carbon*, Vol. 80, pp 629-639, 2014. (doi: 10.1016/j.carbon.2014.09.006).

[13] Y.-N. Liu, M. Li, Y. Gu, Y. Zhang, Q. Li, and Z. Zhang. "Ultrastrong carbon nanotube/bismaleimide composite film with super-aligned and tightly packing structure". *Composites Science and Technology*, Vol. 117, pp 176-182, 2015. (doi: 10.1016/j.compscitech.2015.06.014).

[14] C. Jolowsky, R. Sweat, J. G. Park, A. Hao, and R. Liang. "Microstructure evolution and self-assembling of CNT networks during mechanical stretching and mechanical properties of highly aligned CNT composites". *Composites Science and Technology*, Vol. 166, pp 125-130, 2018. (doi: 10.1016/j.compscitech.2018.04.003).

[15] X. Wang, Q. Jiang, W. Xu, W. Cai, Y. Inoue, and Y. Zhu. "Effect of carbon nanotube length on thermal, electrical and mechanical properties of CNT/bismaleimide composites". *Carbon*, Vol. 53, 145-152, 2013. (doi: 10.1016/j.carbon.2012.10.041).

[16] I. Y. Stein and B. L. Wardle. "Mechanics of aligned carbon nanotube polymer matrix nanocomposites simulated via stochastic three-dimensional morphology". *Nanotechnology*, Vol. 27, pp 035701, 2016. (doi: 10.1088/0957-4484/27/3/035701).

[17] I. Y. Stein, D. J. Lewis, and B. L. Wardle. "Aligned carbon nanotube array stiffness from stochastic three-dimensional morphology". *Nanoscale*, Vol. 7, pp 19426-19431, 2015. (doi: 10.1039/C5NR06436H).

[18] Y. Bai, R. Zhang, X. Ye, Z. Zhu, H. Xie, B. Shen, D. Cai, B. Liu, C. Zhang, Z. Jia, S. Zhang, X. Li, and F. Wei. "Carbon nanotube bundles with tensile strength over 80 GPa". *Nature Nanotechnology*, Vol. 13, pp 589-595, 2018. (doi: 10.1038/s41565-018-0141-z).

[19] D. Puglia, L. Valentini, I. Armentano, and J. Kenny. "Effects of single-walled carbon nanotube incorporation on the cure reaction of epoxy resin and its detection by Raman spectroscopy". *Diamond Related Materials*, Vol. 12, pp 827, 2003. (doi: 10.1016/S0925-9635(02)00358-8).

[20] M. A. Bissett, M. Tsuji, and H. Ago. "Strain engineering the properties of graphene and other two-dimensional crystals". *Physical Chemistry Chemical Physics*, Vol. 16, pp 11124-11138, 2014. (doi: 10.1039/C3CP55443K).

[21] J.-P. Salvetat, J.-M. Bonard, N. H. Thomson, A. J. Kulik, L. Forro, W. Benoit, and L. Zuppiroli. "Mechanical properties of carbon nanotubes". *Applied Physics A*, Vol. 69, pp 255-260, 1999. (doi: 10.1007/s003390050999).

[22] H. Cebeci, R. Guzman de Villoria, A. J. Hart, and B. L. Wardle. "Multifunctional properties of high volume fraction aligned carbon nanotube polymer composites with controlled morphology". *Composites Science and Technology*, Vol. 69, pp 2649-2656, 2009. (doi: 10.1016/j.compscitech.2009.08.006).

[23] D. Handlin, I. Y. Stein, R. Guzman de Villoria, H. Cebeci, E. M. Parsons, S. Socrate, S. Scotti, and B. L. Wardle. "Three-dimensional elastic constitutive relations of aligned carbon nanotube architectures". *Journal of Applied Physics*, Vol. 114, pp 224310, 2013. (doi: 10.1063/1.4842117).

[24] B. J. Briscoe, L. Fiori, and E. Pelillo. "Nano-indentation of polymeric surfaces". *Journal of Physics D: Applied Physics*, Vol. 31, pp 2395-2405, 1998. (doi: 10.1088/0022-3727/31/19/006).

[25] J. Gair. "Nanotube-matrix interplay and tunability in ultrahigh volume-fraction aligned carbon nanotube poly (urethane-urea) nanocomposites". Ph.D. Thesis, Dept. of Mech. Eng., University of Maryland, 2017. (https://dspace.mit.edu/handle/1721.1/116598)